Entrapped Gas and Process Parameter-Induced Porosity Formation in Additively Manufactured 17-4 PH Stainless Steel

Debomita Basu, Ziheng Wu, John L.L. Meyer, Elizabeth Larson, Robin Kuo, and Anthony Rollett

Porosity is one of the most significant obstacles to widescale adoption of additive manufacturing since it acts as a stress concentrator that negatively impacts mechanical properties. Suboptimal process parameters and entrapped gas content in powder feedstock are two factors that can induce porosity in additively manufactured parts. This study utilizes laser diffraction, optical and scanning electron microscopy, and micro-x-ray computed tomography to study how four powders with varied entrapped gas concentrations and gas atomization environments create parts with different densities. Process maps of the four 17-4 PH stainless steel powders used in the EOS M 290 laser powder bed fusion machine, were developed. Furthermore, this paper also discusses how process parameters interact with the powder-entrapped gas porosity to influence the in-part porosity and the Charpy toughness of the as-built components.

1. Introduction

Additive manufacturing (AM) has been of great interest in recent years due to the growth of commercially available systems and advantages these processes provide. Some of these advantages include design freedom with reduced need for expensive or subtractive toolpaths, high material utilization, and a simplified supply chain with reduced lead times and warehousing costs. The excellent properties of 17-4 PH have proven attractive for AM of parts for novel applications. Precipitation-hardened steels are widely used as structural materials and have been used in marine environments, power plants, and chemical industries due to their superior corrosion resistance and strength in moderate and elevated temperatures (Ref 1, 2). 17-4 PH steel in particular is a martensitic precipitation hardening steel that has been used in aerospace

---

Debomita Basu and Ziheng Wu have contributed equally

Debomita Basu, Ziheng Wu, Robin Kuo, and **Anthony Rollett**, Department of Materials Science & Engineering, Carnegie Mellon University, 5000 Forbes Ave, Pittsburgh, PA 15213; **John L.L. Meyer**, Carpenter Technology Corporation, 101 West Bern Street, Reading, PA 19601; and 6K Inc., 25 Commerce Way, N. Andover, MA 01845; **Elizabeth Larson**, Carpenter Powder Products, 500 Park East Drive, Woonsocket, RI; and Ultra Fine Specialty Products, 500 Park East Drive, Woonsocket, RI. Contact e-mail: dbasu@andrew.cmu.edu.

and defense applications such as heavy load components as fasteners, gears, and valves (Ref 3, 4).

In this study, four lots of gas-atomized 17-4 PH stainless steel powder, with entrapped gas porosity levels intentionally varied beyond those typically seen in gas atomized powder, were characterized and used for L-PBF builds. AM parameters, namely laser power, laser scan speed, and hatch spacing, were varied to develop process maps to identify regions of dominant porosity formation mechanisms and to determine the ability of proper AM parameter selection to mitigate powder-induced porosity from even abnormally porous powder.

Introductory overviews of AM and the L-PBF process are readily available from many sources (Ref 5, 6). Just as cast, wrought, or conventional powder metallurgy materials may have defects specific to their processing routes, AM processes can introduce defects that must be accounted for when planning process parameters for a build. One of the major defects in AM materials is porosity. Porosity can arise from a variety of process parameters, which may be detrimental to mechanical properties since pores act as stress concentrators (Ref 7). In L-PBF, the most common forms of porosity result from suboptimal process parameters, forming defects such as lack-of-fusion (LOF) and keyhole porosity. Although research has been conducted in this area to study the relationship of process variables between systems and alloys across different metal AM technologies, the role of parameter selection on the resultant AM defect distribution is not well understood. In addition to parameter choices, powder feedstock can be another source of porosity due to the irregular particle morphology (Ref 8), entrapped gas content (Ref 9, 10), and atomization environment (Ref 11). General literature on the effect of process parameters likely to result in keyholing, lack-of-fusion, and balling defects on porosity is available (Ref 12-17).

Process maps can be used to identify process windows, which indicate desirable process parameter ranges for the materials being used (Ref 18). Process windows are easy visuals that can be used to compare buildability in the different materials used in AM. They are a crucial tool in studying how

to expand and better utilize process space as they map process outcomes in terms of process variables (Ref 19-21). A common type of process map used to study L-PBF is the power–velocity (P-V) process map, where all other build parameters are held at fixed values and only the laser power and velocity are varied. In this work, process maps are used to show how porosity changes with laser power and laser velocity.

To date, gas atomization supplies the largest volume of powder for AM. Since this stochastic process utilizes high-pressure inert gas, a small amount of particles, dependent on particle size and processing, contain entrapped gas pores (Ref 22, 23). Residual porosity in the powder feedstock may cause powder-induced porosity in the as-built part and is another factor to consider when choosing appropriate powder feedstock (Ref 24). When using typical gas atomized powder in most applications, the powder-induced porosity content is typically negligible and plays a minor contribution to mechanical properties. This study used several powders with controlled porosity content levels that were intentionally set above the level typical of atomized powder to determine the effect of entrapped gas porosity on final AM parts.

Utilizing an argon or nitrogen atomization environment can affect both the resulting microstructure (Ref 2, 25) and the number of pores observed in 17-4 PH steel powders (Ref 11). Janowski et al. (Ref 11) studied the effect of atomizing and backfill environments on the frequency of hollow particles observed in the resulting powders. They concluded that the changes to this frequency as a function of atomizing gas were not caused by physical effects upon the atomization process, but rather by differences in the chemical behavior of the gas-metal system. More specifically, they proposed that the gas solubility and diffusivity of argon and nitrogen in metals vary. The solubility of nitrogen increases when decreasing temperature through the liquidus and solidus, while inert gases such as argon demonstrate low solubility in both liquid and solid 304 stainless steel. From this information, it becomes evident that soluble nitrogen gas that is trapped in molten metal will tend to remain soluble and diffuse throughout the system, while entrapped argon will remain as gas enclosing bubbles. Therefore, atomizing the material with a gas that is soluble in the metal may reduce the frequency of hollow particles.

AM can often create voids, high surface roughness, residual stresses, and anisotropic microstructures, which can affect the overall mechanical behavior of the final parts. There have been some studies conducted on porosity in AM parts and the subsequent effects on mechanical properties. Solberg et al. (Ref 26) conducted a study on the fatigue behavior of selective laser-melted 316L stainless steel to investigate the effects of surface roughness and porosity and found that in high-cycle fatigue conditions, specimens failed from surface defects while at high load levels (> 275 MPa), specimens failed from internal defects. Another study (Ref 27) observed that nonporous specimens fabricated via AM methods demonstrated similar tensile strength and behavior to wrought specimens. However, porous samples had considerably lower elongation failure due to elevated stresses facilitating crack propagation. While small amounts of porosity do not significantly impact strength and ductility in static loading conditions, with increasing porosity, a reduction in strength and ductility is observed with failures initiating at the largest pores. In most studies, it was shown that ductility is more strongly influenced by the porosity than the strength. The proximity of pores to the surface is especially important because these near-surface pores are more likely to be crack initiators. If these pores are sufficiently large, they may lead to part failure (Ref 28).

2. Methods

2.1 Fabrication

The fabrication was carried out using an EOS M290 L-PBF machine at Carnegie Mellon University. The part files were prepared using Materialise Magics (Ref 29), and the parameters were assigned in EOSPrint (Ref 30). To study the effects of powder gas entrapment and fabrication environment, a total of five builds were fabricated in either an argon or nitrogen environment using a nominal layer thickness of 40 μm. There were four different 17-4 PH powder lots of the same chemical composition with different entrapped porosity levels intentionally varied outside of normal production ranges. Each build contained 25 rectangular prisms with dimension of $15(L) \times 10(W) \times 10(H)$ mm^3 where the laser power, laser scan speed, and hatch spacing were systematically varied. Note that the parameter selection started with a commonly used baseline parameter set for 17-4 PH stainless steel which is 195 W and 750 mm/s.

To explore the process window, a 4 by 5 experimental matrix shown in Table 1 with 20 total combinations was chosen in the P-V space at a hatch spacing of 120 μm. Parameters were established in this way to facilitate comparison between parts fabricated at the same laser powers or velocities. The Rosenthal equation (Ref 31) was used to estimate the melt pool size, and the lack-of-fusion criterion developed by Tang et al. (Ref 32)

Table 1 Processing parameters used in fabrication of the block specimens in all powder/environment build conditions featured in this work

Laser power (W)	Laser velocity (mm/s)	Hatch spacing (μm)
150	600	120
150	800	120
150	1000	120
150	1200	120
200	600	120
195	750	120
200	1000	120
200	1200	120
250	600	120
250	800	120
250	1000	120
250	1200	120
300	600	120
300	800	120
300	1000	120
300	1200	120
350	600	120
350	800	120
350	1000	120
350	1200	120
195	750	60
195	750	90
195	750	150
200	1200	60
200	1200	90

was used to identify the lack-of-fusion boundary. These models were used to inform parameter selection for the experimental matrix to ensure that the selected matrix sufficiently covered areas of the process space to capture different defect formation mechanisms, e.g., lack-of-fusion and powder-induced porosity. Other combinations, with laser power < 150 W or velocity < 600 mm/s, were not included as they would have resulted in impractically large levels of lack-of-fusion defects or commercially unviable manufacturing velocities, respectively.

2.2 Characterization

Prior to fabrication, scanning electron microscopy (SEM) was used to visualize the morphology of the powder particles and laser diffraction was used to acquire measurements of particle size distribution. After the samples were built, the rectangular prisms were first cut along the building direction to show the 15(L) × 10(H) mm^2 cross section using wire electrical discharge machining (EDM) and sequentially polished to remove the machined surface using silicon carbide paper, diamond paste, and colloidal silica. The resulting cross-sectional images, shown in Fig. 1, were then captured on a Leica DM750M optical microscope. These images were then fed into Fiji (Ref 33) image analysis software to perform segmentation, shape measurement, and size quantification of pores.

X-ray microcomputed tomography (μ × XCT) was utilized to study pore morphology in 3D since this tool is often used to analyze additively manufactured parts for porosity (Ref 17). μ × XCT was performed at the 2-BM beamline of the Advanced Photon Source at Argonne National Lab. Their setup used a pink beam to illuminate the specimen with an exposure of 0.024 s, an imaging volume of 1.55(L) × 1.55(W) × 1.41(H) mm^3, and spatial resolution of 0.69 μm/pixel with 5× objective magnification. The collected sinograms were fed into TomoPy 0.0.3 to reconstruct the data, and the resulting segmentation, analysis, and visualization were performed in FEI Avizo 9.1.1.

3. Results

3.1 Analysis of Gas-Atomized 17-4 PH Powder

Four different batches of 17-4 PH powders are used in this study. They are nitrogen-atomized N2 powder and the argon-atomized Ar-1, Ar-2, and Ar-3 powders. The porosity levels were intentionally varied to abnormally elevated levels through powder production process modification. As shown in Fig. 2, most of the powder particles have a spherical morphology with some minor satelliting and agglomerates.

To measure the size distribution of the powders, laser diffraction was performed per ASTM B822 (Ref 34) on a Microtrac S3000 in SA150 mode. The results of this analysis are shown in Table 2.

The reconstructed μXCT data analysis showed that the Ar-2 and Ar-3 powders have higher entrapped gas concentrations when compared to Ar-1 and the N2 powders. When counting spherical pores [anisotropy < 0.6 as used in (Ref 35)], the solid fraction of Ar-1, Ar-2, Ar-3, and N2 powders is 99.99%, 99.93%, 99.86%, and 99.99%, respectively. More detail on how this was completed can be found in (Ref 35), which used the same powders and processing conditions as those used in this work.

3.2 Fabrication in L-PBF

The argon-atomized powders were used in an argon environment, while the nitrogen-atomized powders were used in both an argon environment and a nitrogen environment. A common nominal powder layer thickness of 40 μm was used for all builds without observable spreading defects. As mentioned above, the porosity of the rectangular prisms fabricated in the five build conditions was quantified by analyzing metallographic cross sections. Another method of measuring the density of the parts is the Archimedes' method. The microscopy method was used in favor of the Archimedes' method as significant differences between the two approaches for sufficiently dense parts are less than 1% (Ref 36, 37). Figure 3 summarizes the porosity concentration with a color bar at each laser power and laser velocity combinations for all builds using a fixed hatch spacing of 120 μm. Samples containing greater than or equal to 1% porosity are marked in red, while the other samples are at porosity contents less than 1%. The colormap was altered to demonstrate more contrast at these lower levels of porosity.

Some of the block samples fabricated in the Ar-2 powder were selected for μXCT analysis to determine the effect of the process parameters on pore morphology, as shown in Fig. 4. As per the discussion in Ref 35, an anisotropy value of 0.6 was selected as a threshold to determine whether porosity in as-built parts originated from the powder feedstock (anisotropy < 0.6) or occurred as a result of the selected process parameters (anisotropy > 0.6).
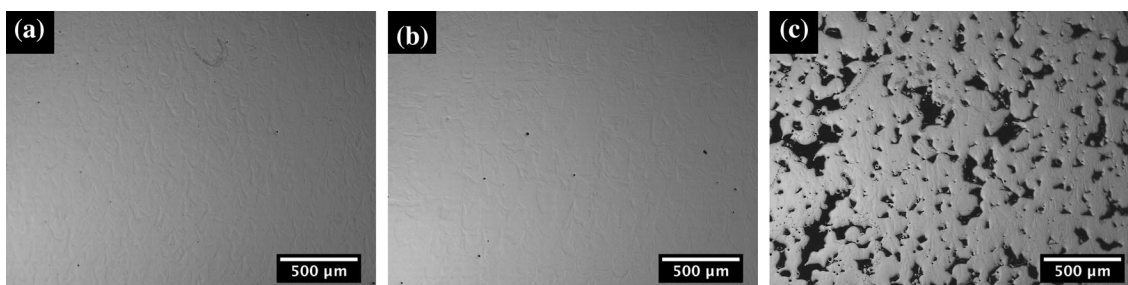
Figure 1 An example of optical images used in porosity measurements utilizing a traditional metallographic cross-sectioning approach. The optical micrographs are sampled from Ar-3 specimens fabricated using (a) nominal parameters (750 mm/s and 195 W), (b) near-keyholing parameters (600 mm/s and 350 W) and (c) lack-of-fusion parameters (1200 mm/s and 150 W)
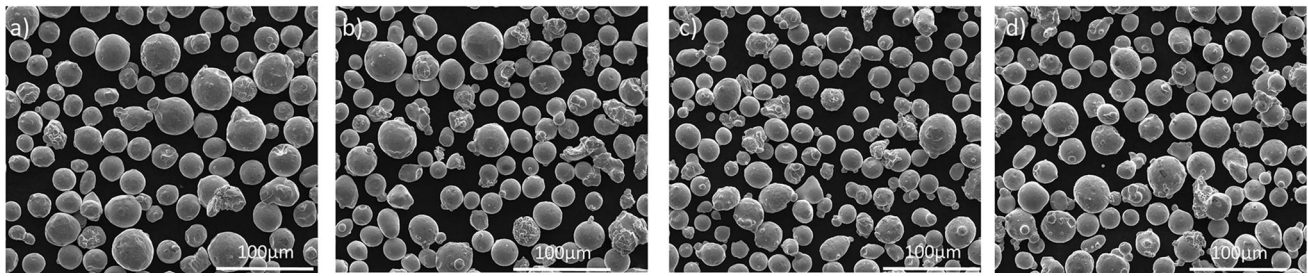
Figure 2 SEM micrographs of (a) N2, (b) Ar-1, (c) Ar-2, and (d) Ar-3 gas-atomized 17-4 PH stainless steel powders

Table 2 Size statistics of four lots of gas-atomized 17-4PH stainless steel powder (volume weighted)

Measurement (μm)	N2	Ar-1	Ar-2	Ar-3
d_{10}	22.2	18.3	16.2	19.0
d_{50}	34.3	29.6	26.4	31.4
d_{90}	52.0	43.9	42.6	48.1

3.3 Mechanical Testing Results

In addition to the density experiments conducted with the four powders, Charpy bar specimens were printed with the Ar-2 powder as per the parameters specified in Table 3.

The samples were stress-relieved at 600 ºC for 2 hours and then machined off the plate via wire EDM. They were then subjected to the H900 heat treatment, which specifies solution annealing at 1040 °C for 30 minutes with subsequent air cooling to room temperature. Afterward, the samples were aged at 480 °C for one hour and air-cooled. The resulting impact toughness values are shown in Fig. 5 as a function of the densities of the parts.

4. Discussion

This work aimed to study the porosity in parts fabricated via L-PBF, considering porosity sources such as the laser parameters used and the entrapped gas in powder feedstock. The powders primarily differed in their atomization environments. Table 2 shows that all powder lots have d_{10}, d_{50}, and d_{90} values within a common tolerance of ± 5 μm, while the discussion from "Analysis of Gas-Atomized 17-4 PH Powder" section mentions that the order of the powders from least porous to most is N2 < Ar-1 < Ar-2 < Ar-3, suggesting an influence of the atomizing environment.

While the porosity maps in Fig. 3 do not reveal the keyhole boundary due to process parameter selection, the lack-of-fusion boundary can be easily identified for each build condition and match what is expected based on the LOF criterion from Tang et al. (Ref 32). While some parameters on this boundary yield a slightly higher porosity content than others, using different powders could shift this boundary and the corresponding porosity values. With proper powder selection, laser velocities up to 1,200 mm/s can potentially be employed to accelerate the fabrication process.

Since the process window for all five builds are similar, it is not surprising that a general trend was observed between the entrapped gas porosity content of the powder and the resultant in-part porosity. The parts fabricated with Ar-1 resulted in less porosity than those made in Ar-2, which were denser than the Ar-3 parts, supporting the trend in powder porosity from "Analysis of Gas-Atomized 17-4 PH Powder" section. The nitrogen-atomized powder generally created denser parts when it was fabricated in a nitrogen environment compared to an argon environment, but the porosity difference is too close to draw a definitive conclusion. This may possibly be explained by the results of Janowski et al. (Ref 11) that address the higher solubility of nitrogen in stainless steel as compared to argon.

Figure 5 shows impact toughness and density values for Charpy specimens fabricated in the Ar-2 powder as per the parameters from Table 3. It is important to note that Charpy impact tests are not very sensitive to porosity present in the test samples due to the high strain rate. However, entrapped gas porosity has been shown to affect the fatigue properties of a sample (Ref 38). The porosity measurements from the Charpy bar samples are subject to variability due to the image processing measurement methods, and error bars were calculated and applied from the standard deviation of the impact toughness and density measurements. Although a definitive trend is not apparent from Fig. 5, it seems that parts with densities above 99.7% tend to have higher impact toughness values than less dense specimens. The stripe melting strategy may have been beneficial to the impact toughness as evidenced by the difference between samples 1 and 2. Excessively large and small hatch spacings may induce large variabilities in densities as evidenced by sample 3 (in comparison with sample 1) and sample 6 (in comparison with sample 5), highlighting the importance of selecting an appropriate value for this parameter. Hatch spacing should be determined based on the expected melt pool width in order to ensure the melt pools overlap properly. Sample 3 and sample 6 show that too small or too large of a hatch spacing in comparison with the expected melt pool width may result in a greater variability in density. Sample 7 was fabricated with the highest build rate and was denser than sample 3 most likely due to the higher power used. The densities of all the samples with the exception of sample 3 are greater than 99%, which would correspond to the green, cyan, or blue colors according to the color maps presented in Fig. 3.

While the trends in part densities and the powder densities are nontrivial, different parameters demonstrated different sensitivities to powder-entrapped gas-induced porosity. To examine how the sensitivity varies, Fig. 6 shows the difference of porosity values between the Ar-1 and Ar-3 builds for each P-V combination within the process window against the energy density, as calculated by Equation 1 (volumetric power input) (Ref 32),

$$\text{Energy density} = \frac{P}{VHL} \qquad \text{(Eq 1)}$$
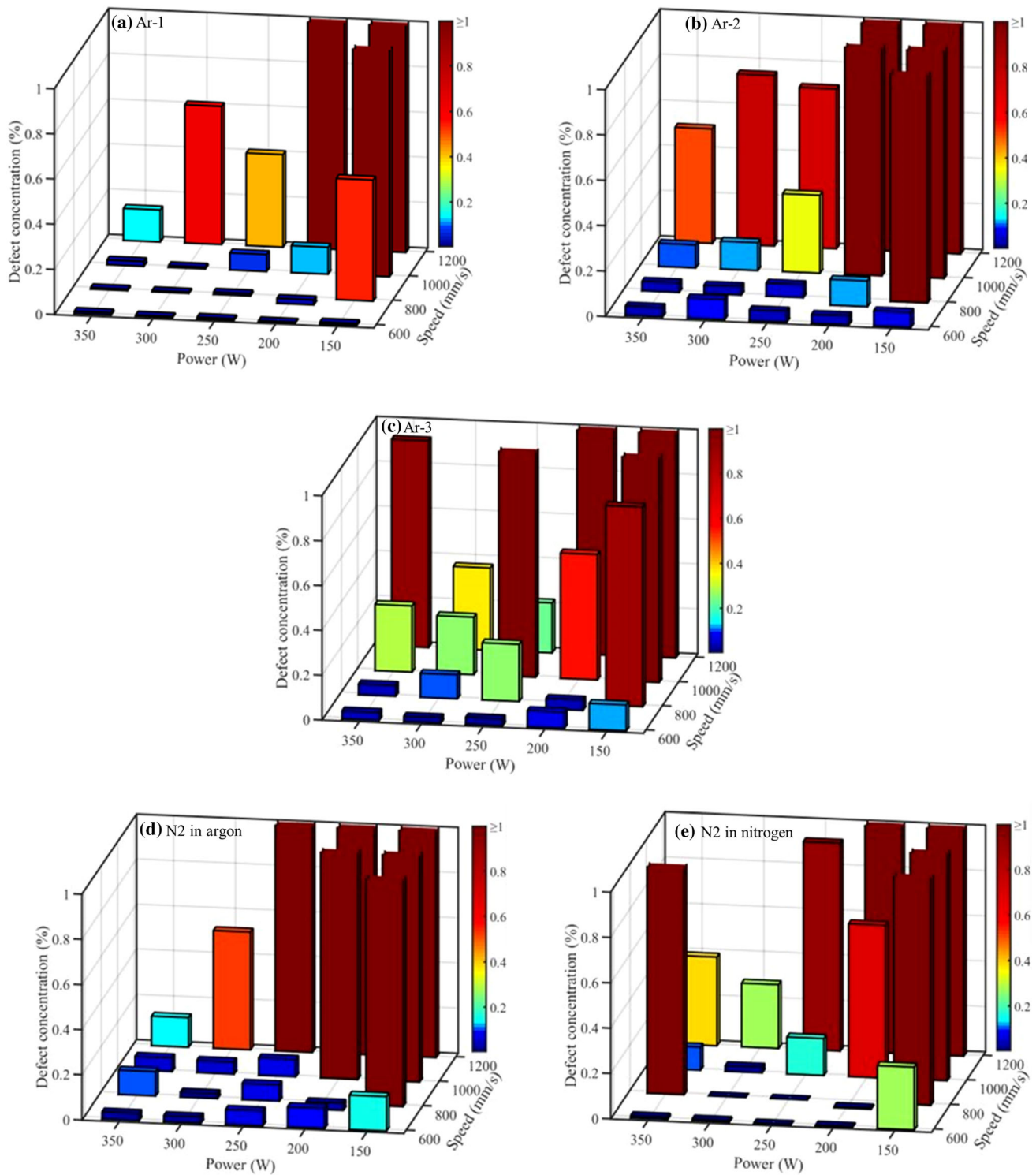
Figure 3 Porosity map of parts using (a-c) argon-atomized powders built in an argon environment, (d) N2 powder built in argon environment, and (e) N2 powder built in nitrogen environment

where P is laser power, V is laser velocity and H is hatch spacing, and L is layer thickness. This difference in porosity between the two builds is used as a measure of the powder porosity sensitivity since both powders were used in identical build conditions. The highlighted region in Fig. 6 corresponds to a subset of parameters in P-V space in the porosity maps where LOF is not occurring. At these intermediate energy densities, the porosity difference between

the Ar-1 and Ar-3 builds can range from .02 to .8%. Large porosity differences due to powder selection could potentially push samples over the density threshold of 99.7%, shown in Fig. 5, leading to better impact toughness values with lower variability in both density and impact toughness. This suggests that altering the energy density of the processing parameters may reduce the impact of the entrapped gas porosity on the final part porosity.
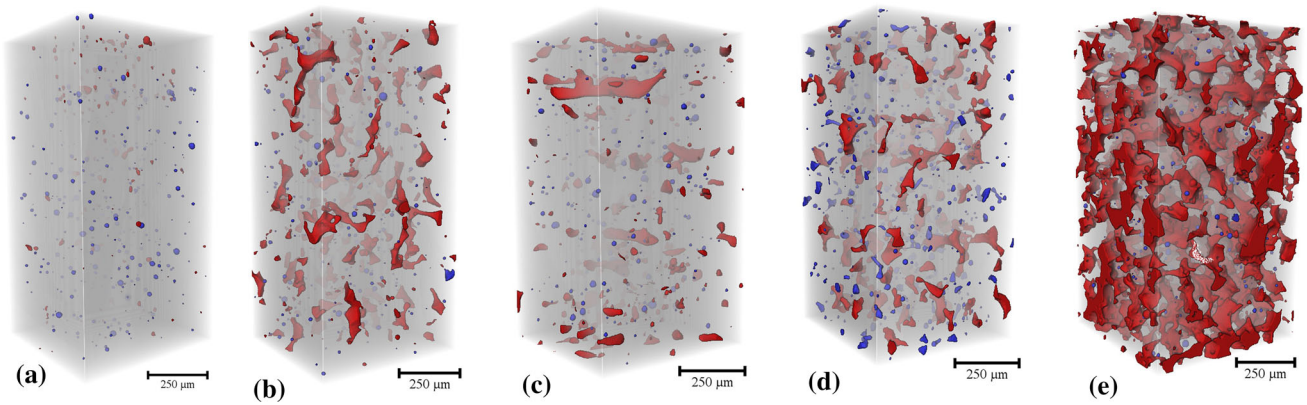
Figure 4 μXCT reconstructions of AM specimens fabricated using the Ar-2 powder in an argon building environment with parameters of (a) 750 mm/s, 195 W, and 120-μm hatch spacing, (b) 750 mm/s, 195 W, and 150-μm hatch spacing, (c) 1200 mm/s, 350 W, and 120-μm hatch spacing, (d) 1000 mm/s, 200 W, and 120-μm hatch spacing, and (e) 1200 mm/s, 150 W, and 120-μm hatch spacing. Note that the more spherical pores (anisotropy < 0.6) are highlighted in blue and the irregularly shaped pores (anisotropy > 0.6) are highlighted in red (Color figure online).

Table 3 Parameters used to fabricate Charpy bar specimens in the Ar-2 17-4PH powder

Sample	Power (W)	Velocity (mm/s)	H (mm)	Rationale
#1	195	750	120	Baseline parameter set
#2	195	750	120	Baseline parameter set with stripe melting strategy
#3	195	750	150	Increased hatch spacing for baseline combination
#4	300	1000	120	Comparable pore distribution to baseline parameter set with increased power and velocity
#5	300	800	120	Parameter set that yielded highest density
#6	300	800	60	Decreased hatch spacing of previous sample to acquire higher density
#7	350	1200	120	Fastest build rate
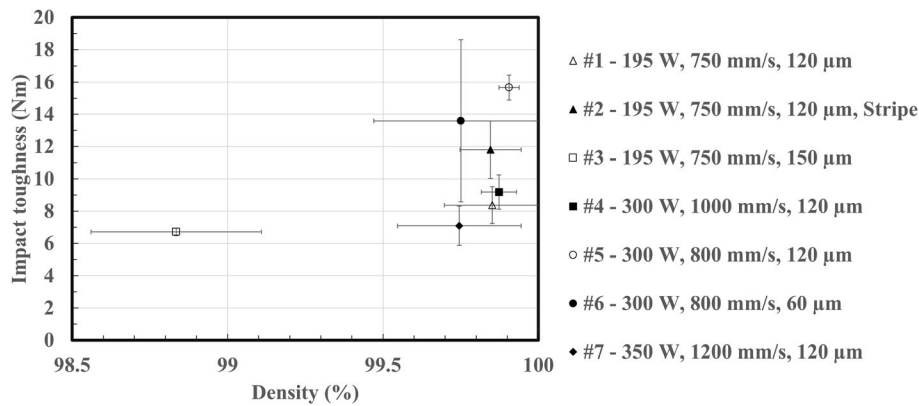
Figure 5 Charpy impact results for specimens fabricated with Ar-2 17-4 PH powder as per Table 3

In this region of relatively lower energy density, the parameters showed higher sensitivity (higher difference) to powder porosity. This may be connected to melt pool geometry as lower energy density parameters typically result in smaller melt pool size and less remelting which creates unfavorable conditions for pores to escape by limiting the time that pores can travel in the liquid metal. In contrast, parameters exhibiting higher energy densities showed low sensitivity to powder-entrapped gas-induced porosity.

To further investigate how melt pool geometry may affect the ability of pores to escape, markers of variable sizes are used in Figure 7 to represent the porosity difference between the Ar-1 and Ar-3 builds. This difference was plotted against the energy density of the parameters and melt pool aspect ratio shown in Equation 2 (melt pool aspect ratio as derived by the Rosenthal equation) (Ref 31):

$$\frac{L}{W} = \sqrt{\frac{\in eQV}{32\pi k\alpha\left(T_{melt} - T_{preheat}\right)}} \tag{Eq 2}$$

where L is melt-pool length, W is melt-pool width, $\in$ is laser absorptivity, Q is laser power, V is laser velocity, k is thermal conductivity, α is thermal diffusivity, T_{melt} is the melting temperature of the alloy, and $T_{preheat}$ is the preheat temperature
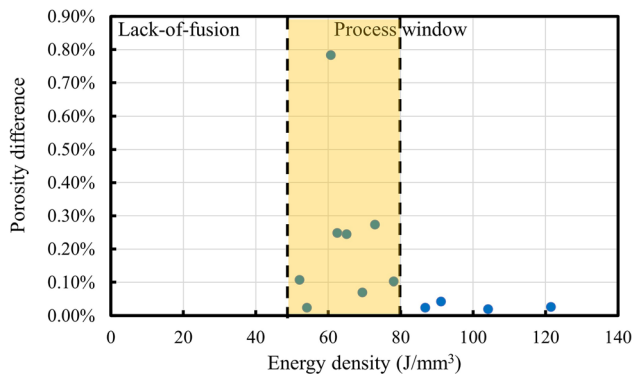
Figure 6 The difference of porosity values at each power–velocity combination within the process window between the Ar-1 and Ar-3 builds
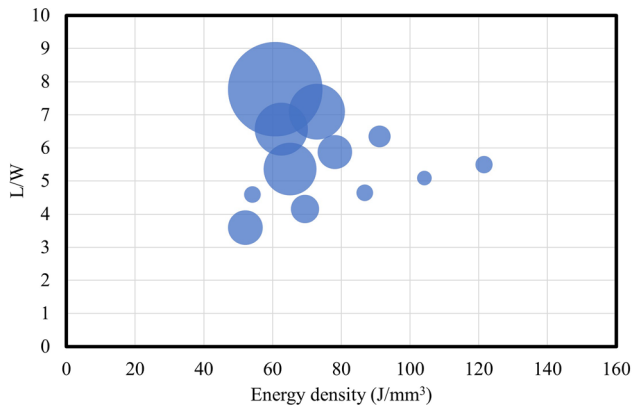
Figure 7 The difference of porosity values at each power–velocity combination within the process window between the Ar-1 and Ar-3 builds plotted against melt-pool shape and the corresponding energy density

of the built plate. As shown in Fig. 7, the parameters show higher sensitivity to powder porosity as the L/W ratio increases at intermediate energy densities. This suggests that the shape of the melt pool may play a role in how easily pores escape from the melt pool and that a shorter melt pool may facilitate this escape more than a longer one.

μXCT was used to show the spatial distribution of porosity in some as-built Ar-2 parts as demonstrated in Fig. 4. Some of these parameter sets induce irregularly shaped and interconnected lack-of-fusion pores. The various pore morphologies shown in Fig. 4 can be attributed to the parameters selected. The high hatch spacing selected in Fig. 4(b) resulted in insufficient melt pool overlap, whereas the potential bead up of the melt pool at high powers and velocities in Fig. 4(c) may have created excessively rough surfaces that aggravate the spreading of powder and melting of the subsequent layer. While Fig. 4(d) is a transition parameter, increasing the travel velocity and decreasing the power result in insufficient heat input as can be observed in Fig. 4(e). In the case of lack-of-fusion shown in Fig. 4(e), the volume ratio of nonspherical porosity over spherical porosity reaches 150.

There are several things to take away from these experiments that can influence the design of AM experiments and applications. The material feedstock is very important since the porosity from the powders affects the porosity of the final part.

This might suggest that AM processes should exclusively use low porosity powders; however, this greatly increases the cost of the materials and therefore the AM process. This work shows that powders with higher entrapped gas concentrations can be used to generate fully dense parts but require high energy density parameters to do so. This may facilitate the adoption of cost-effective powders for L-PBF.

5. Conclusions

This study investigated porosity as induced by process parameters and powder feedstock in a L-PBF AM process with 17-4 PH stainless steel. Three of the powder feedstocks were atomized with and used to fabricate parts in argon, while the fourth powder was atomized with nitrogen and fabricated with both argon and nitrogen environments. The main findings were as follows:

Process windows for each of the four powders have been explored, revealing the lack-of-fusion boundary in the lower power and higher velocity corner of process space.

Adjusting process parameters can significantly affect pore morphology for process-induced porosity as shown by μXCT.

Utilizing process parameters with higher energy densities may reduce the effect of entrapped gas porosity in parts.

When appropriate hatch spacing values are used in relation to the expected melt pool width, samples exhibiting densities > 99.7% may see increased Charpy impact toughness values.

Melt pool geometry may play a role in how easily pores can escape. Longer, narrower melt pools may trap more pores and shorter, wider melt pools may facilitate pores escaping.

Declarations

Conflict of interest

The authors declare that they have no conflict of interest.

References

1. D. C. Ludwigson and A. M. Hall, The physical metallurgy of precipitation-hardenable stainless steels, 1959

2. L.E. Murr et al., Microstructures and Properties of 17–4 PH Stainless Steel Fabricated by Selective Laser Melting, *J. Mater. Res. Technol.*, 2012 https://doi.org/10.1016/S2238-7854(12)70029-7

3. X. Lin, Y. Cao, X. Wu, H. Yang, J. Chen and W. Huang, Microstructure and Mechanical Properties of Laser Forming Repaired 17–4PH Stainless Steel, *Mater. Sci. Eng. A*, 2012 https://doi.org/10.1016/j.msea.2012.05.095

4. Z. Hu, H. Zhu, H. Zhang and X. Zeng, Experimental Investigation on Selective Laser Melting of 17–4PH Stainless Steel, *Opt. Laser Technol.*, 2017 https://doi.org/10.1016/j.optlastec.2016.07.012

5. I. Gibson, D.W. Rosen and B. Stucker, *Additive Manufacturing Technologies: Rapid Prototyping to Direct Digital Manufacturing*, Springer, 2010

6. W.E. Frazier, Metal Additive Manufacturing: A Review, *J. Mater. Eng. Perform.*, 2014, **23**(6), p 1917–1928. https://doi.org/10.1007/s11665-014-0958-z

7. W.D. Callister, M*aterials Science and Engineering: An Introduction*, 8th ed., W.D. Callister, D.G. Rethwisch, Ed., Wiley, 1985. https://www.worldcat.org/title/materials-science-and-engineering-an-introduction/oclc/401168960

8. S.P. Narra et al., Use of Non-Spherical Hydride-Dehydride (HDH) Powder in Powder Bed Fusion Additive Manufacturing, *Addit. Manuf.*, 2020 https://doi.org/10.1016/j.addma.2020.101188

9. R. Cunningham et al., Analyzing the Effects of Powder and Post-Processing on Porosity and Properties of Electron Beam Melted Ti-6Al-4V, *Mater. Res. Lett.*, 2017 https://doi.org/10.1080/21663831.2017.1340911

10. S. Tammas-Williams, H. Zhao, F. Léonard, F. Derguti, I. Todd and P.B. Prangnell, XCT Analysis of the Influence of Melt Strategies on Defect Population in Ti-6Al-4V Components Manufactured by Selective Electron Beam Melting, *Mater. Charact.*, 2015 https://doi.org/10.1016/j.matchar.2015.02.008

11. G.M. Janowski, F.S. Biancaniello and S.D. Ridder, Beneficial Effects of Nitrogen Atomization on an Austenitic Stainless Steel, *Metall. Trans. A*, 1992 https://doi.org/10.1007/BF02663435

12. F. Lu, X. Li, Z. Li, X. Tang and H. Cui, Formation and Influence Mechanism of Keyhole-Induced Porosity in Deep-Penetration Laser Welding Based on 3D Transient Modeling, *Int. J. Heat Mass Transf.*, 2015, **90**, p 1143–1152. https://doi.org/10.1016/j.ijheatmasstransfer.2015.07.041

13. S.M.H. Hojjatzadeh et al., Pore Elimination Mechanisms During 3D Printing of Metals, *Nat. Commun.*, 2019 https://doi.org/10.1038/s41467-019-10973-9

14. B.E. Carroll, T.A. Palmer and A.M. Beese, Anisotropic Tensile Behavior of Ti-6Al-4V Components Fabricated with Directed Energy Deposition Additive Manufacturing, *Acta Mater.*, 2015, **87**, p 309–320. https://doi.org/10.1016/j.actamat.2014.12.054

15. A.M. Beese and B.E. Carroll, Review of Mechanical Properties of Ti-6Al-4V Made by Laser-Based Additive Manufacturing Using Powder Feedstock, *JOM*, 2016, **68**(3), p 724–734. https://doi.org/10.1007/s11837-015-1759-z

16. S.A. Khairallah and A. Anderson, Mesoscopic Simulation Model of Selective Laser Melting of Stainless Steel Powder, *J. Mater. Process. Technol.*, 2014, **214**(11), p 2627–2636. https://doi.org/10.1016/j.jmatprotec.2014.06.001

17. A. du Plessis, I. Yadroitsev, I. Yadroitsava and S.G. Le Roux, "X-Ray Microcomputed Tomography in Additive Manufacturing: A Review of the Current Technology and Applications", 3D Print, *Addit. Manuf.*, 2018, **5**(3), p 227–247. https://doi.org/10.1089/3dp.2018.0060

18. A.M. Rausch, V.E. Küng, C. Pobel, M. Markl and C. Körner, Predictive Simulation of Process Windows for Powder Bed Fusion Additive Manufacturing Influence of the Powder Bulk Density, *Materials (Basel)*, 2017 https://doi.org/10.3390/ma10101117

19. J. Beuth et al., Process mapping for qualification across multiple direct metal additive manufacturing processes, In *24th International Solid Freeform Fabrication Symposium-An Additive Manufacturing Conference, SFF 2013*, 2013, pp. 655–665, https://www.scopus.com/inward/record.uri?eid=2-s2.0-84898470851&partnerID=40&md5=f006d5df1fa420ac078b7619a54b7f5f

20. C. Montgomery, J. Beuth, L. Sheridan, and N. Klingbeil, Process Mapping of Inconel 625 in Laser Powder Bed Additive Manufacturing, In *Solid Freeform Fabrication Proceedings*, 2015, Accessed: Jun. 15, 2017. https://sffsymposium.engr.utexas.edu/sites/default/files/2015/2015-97-Montgomery.pdf

21. J. Gockel and J. Beuth, Understanding Ti-6Al-4V microstructure control in additive manufacturing via process maps, In *24th International SFF Symposium-An Additive Manufacturing Conference, SFF 2013*, 2013

22. B. Zhang, Y. Li and Q. Bai, Defect Formation Mechanisms in Selective Laser Melting: A Review, *Chinese Journal of Mechanical Engineering*, 2017 https://doi.org/10.1007/s10033-017-0121-5 (**(English Edition)**)

23. M.N. Ahsan, A.J. Pinkerton, R.J. Moat and J. Shackleton, A Comparative Study of Laser Direct Metal Deposition Characteristics Using Gas and Plasma-Atomized Ti-6Al-4V Powders, *Mater. Sci. Eng. A*, 2011 https://doi.org/10.1016/j.msea.2011.06.074

24. R. Cunningham et al., Analyzing the Effects of Powder and Post-processing on Porosity and Properties of Electron Beam Melted Ti-6Al-4V, *Mater. Res. Lett.*, 2017, **5**(7), p 516–525. https://doi.org/10.1080/21663831.2017.1340911

25. H. Gu, H. Gong, D. Pal, K. Rafi, T. Starr, and B. Stucker, "Influences of energy density on porosity and microstructure of selective laser melted 17-4PH stainless steel," In *24th International SFF Symposium-An Additive Manufacturing Conference, SFF 2013*, 2013

26. K. Solberg, S. Guan, S.M.J. Razavi, T. Welo, K.C. Chan and F. Berto, Fatigue of Additively Manufactured 316L Stainless Steel: The Influence of Porosity and Surface Roughness, *Fatigue Fract. Eng. Mater. Struct.*, 2019 https://doi.org/10.1111/ffe.13077

27. S.M.J. Razavi, G.G. Bordonaro, P. Ferro, J. Torgersen and F. Berto, Porosity Effect on Tensile Behavior of Ti-6Al-4V Specimens Produced by Laser Engineered Net Shaping Technology, *Proc. Inst. Mech. Eng. Part C J. Mech. Eng. Sci.*, 2018 https://doi.org/10.1177/0954406218813384

28. A. du Plessis, I. Yadroitsava and I. Yadroitsev, Effects of Defects on Mechanical Properties in Metal Additive Manufacturing: A Review Focusing on X-ray Tomography Insights, *Mater. Des.*, 2020 https://doi.org/10.1016/j.matdes.2019.108385

29. "Magics," *Materialise*. Aug. 20, 2019, https://www.materialise.com/en/software/magics

30. "Software Solutions for Additive Manufacturing." https://www.eos.info/systems_solutions/software

31. D. Rosenthal, "Mathematical Theory of Heat Distribution During Welding and Cutting," *Weld. J.*, 1941

32. M. Tang, P.C. Pistorius and J.L. Beuth, Prediction of Lack-of-Fusion Porosity for Powder Bed Fusion, *Addit. Manuf.*, 2017, **14**, p 39–48. https://doi.org/10.1016/j.addma.2016.12.001

33. J. Schindelin et al., Fiji: An Open-Source Platform for Biological-Image Analysis, *Nat. Methods*, 2012 https://doi.org/10.1038/nmeth.2019

34. ASTM B822-17, Standard test method for particle size distribution of metal powders and related compounds by light scattering, *ASTM Int. West Conshohocken, PA*, 2017

35. Z. Wu et al., Study of Powder Gas Entrapment and Its Effects on Porosity in 17–4 PH Stainless Steel Parts Fabricated in Laser Powder Bed Fusion, *JOM*, 2021 https://doi.org/10.1007/s11837-020-04491-z

36. A.B. Spierings, M. Schneider and R. Eggenberger, Comparison of Density Measurement Techniques for Additive Manufactured Metallic Parts, *Rapid Prototyp. J.*, 2011, **17**(5), p 380–386. https://doi.org/10.1108/13552541111156504

37. Z. Sun, X. Tan, S.B. Tor and W.Y. Yeong, Selective Laser Melting of Stainless Steel 316L with Low Porosity and High Build Rates, *Mater. Des.*, 2016 https://doi.org/10.1016/j.matdes.2016.05.035

38. V. D. Le, E. Pessard, F. Morel, and F. Edy, "Influence of porosity on the fatigue behaviour of additively fabricated TA6V alloys," In *MATEC Web of Conferences*, 2018, https://doi.org/10.1051/matecconf/201816502008